*J Mater Sci* (2023) 58:186–198

Chemical routes to materials

# Morphological guidance and proportional control of $Cu_2O$/ZnO core/shell heterojunction with enhanced visible-light-driven photocatalytic performance

Lin Cheng[1], Guosong Wu[1], Diqing Ruan[1], Huaping Wu[2], and Aiping Liu[1,*]

[1] Key Laboratory of Optical Field Manipulation of Zhejiang Province, School of Materials Science & Engineering, Zhejiang Sci-Tech University, Hangzhou 310018, China

[2] Key Laboratory of Special Purpose Equipment and Advanced Processing Technology, Ministry of Education and Zhejiang Province, College of Mechanical Engineering, Zhejiang University of Technology, Hangzhou 310023, China

**Received:** 21 August 2022
**Accepted:** 5 December 2022
**Published online:** 1 January 2023



## ABSTRACT

As a candidate for photocatalyst, the photocatalytic performance of cuprous oxide ($Cu_2O$) is severely restricted by its high charge carrier recombination rate, self-photocorrosion and the uncertainty of crystal plane. In order to improve the photocatalytic performance and deeply analyze the photocatalytic mechanism, the $Cu_2O$ nanocrystals with cubic, cuboctahedral and octahedral structures were combined with n-type ZnO to prepare $Cu_2O$/ZnO heterojunction photocatalysts. The effects of crystal facet of $Cu_2O$ and Zn/Cu ratios on the photocatalytic performances of $Cu_2O$/ZnO heterojunctions were explored into. The results show that the cuboctahedron $Cu_2O$ with {100} and {111} facets exhibits more surprising catalytic performance due to the energy-level difference between the two facets, leading to higher electron–hole pair separation efficiency when compared with the octahedral $Cu_2O$ with {111} facets and cubic $Cu_2O$ with {100} facets. In addition, optimized $Cu_2O$/ZnO heterojunction with appropriate Zn/Cu ratio exhibits the collaborative advantages of the two materials, so the catalytic activity and stability are effectively improved.

Handling Editor: Pedro Camargo.

Address correspondence to E-mail: liuaiping1979@gmail.com; liuap@zstu.edu.cn



https://doi.org/10.1007/s10853-022-08059-x

## GRAPHICAL ABSTRACT

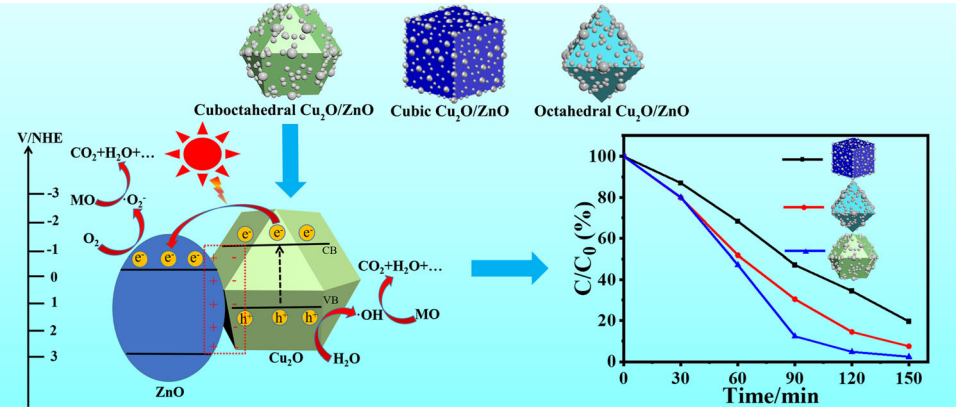


## Introduction

Cuprous oxide ($Cu_2O$) is an attractive semiconductor with a direct bandgap of about 2.2 eV, which can absorb visible light in the solar spectrum, and presents many excellent features, such as large storage capacity, reasonable cost, environmentally friendly and strong molecular oxygen adsorption capacity [1–8]. However, the practical application of $Cu_2O$ as a photocatalyst is still limited due to the difference in catalytic activity of $Cu_2O$ with different morphologies and crystal orientations, relatively high recombination rate of photogenerated charge carriers and self-photocorrosion behavior under light irradiation [9–11]. In order to solution this problem, rational design and construction of heterostructure by using n-type semiconductors with p-type $Cu_2O$ is a viable strategy. The p–n junction with a depletion layer formed in the interfacial region subsequently induces an internal self-built electric field, which promotes the separation of electron–hole pairs and enhances the photocatalytic activity [12, 13]. The p–n junction can accurately and effectively control the separation distance and transmission direction and suppress the recombination of charge carriers. In addition, the n-type materials such as $TiO_2$ [14, 15], $SnO_2$ [16] and ZnO [17–19] can greatly improve the stability of the heterojunction [20, 21]. When comparing the positions of the band gaps of ZnO and $Cu_2O$, it can be noticed that the conduction band minimum of $Cu_2O$ is located more negatively than that of ZnO, and the valence band maximum of ZnO is located more positive than that of $Cu_2O$ [22–24]. The staggered bandgap structures of $Cu_2O$/ZnO heterostructures follow a typical type II mode, which can lead to efficient spatial separation and transfer of electron–hole pairs, reducing internal charge recombination and enhancing photocatalytic activity [25–28]. Furthermore, considering that different crystal facets of $Cu_2O$ have different photocatalytic activities, for low-index facets of $Cu_2O$ crystals, researchers have reached a consensus, namely the average surface energies follow the order as {110} > {111} > {100} [3, 29, 30]. However, the effects of crystal planes and morphologies of $Cu_2O$ on the catalytic activity of $Cu_2O$/ZnO heterojunctions still need to be studied in depth.

Herein, we fabricate $Cu_2O$ nanostructures with adjustable surface morphologies and desired crystal facets, namely cubic $Cu_2O$ with {100} facets (denoted as C-$Cu_2O$), octahedral $Cu_2O$ with {111} facets (denoted as O-$Cu_2O$) and cuboctahedrons $Cu_2O$ with both {111} and {100} facets (denoted as C-O-$Cu_2O$), respectively. Subsequently, $Cu_2O$/ZnO p–n heterojunction with various Zn/Cu ratios is synthesized by a simple and rapid strategy. A facet-dependent photocatalytic behavior for methyl orange (MO) photodegradation is also verified. The optimal design of $Cu_2O$/ZnO p–n heterojunction with excellent photocatalytic activity, improved transport of charge carriers and photostability forebodes a potential

application of this composite material as bright photocatalysts in the fields of photocatalysis, sewage treatment and environmental cleaning.

## Experimental section

### Chemicals

Cupric chloride dihydrate ($CuCl_2{\cdot}2H_2O$), polyvinyl pyrrolidone (PVP K29-32), ascorbic acid (AA), sodium hydroxide (NaOH), trisodium citrate dihydrate ($C_6H_5Na_3O_7{\cdot}2H_2O$), zinc acetate ($Zn(AC)_2{\cdot}2H_2O$), chloroauric acid trihydrate ($HAuCl_4{\cdot}3H_2O$, 99%), Nafion solution and ethanol were purchased from Sigma-Aldrich Co. LLC. of China. All chemicals were analytic grade and used without further purification treatments. Deionized water (> 18 MΩ·cm) was prepared from Q purification system and used throughout all the experiments.

### Synthesis of $Cu_2O$ crystals

$Cu_2O$ crystals with different morphologies were synthesized through a reported process [31] with slight modification. Simply, a certain amount of PVP, 0.18 g of $CuCl_2{\cdot}2H_2O$, 0.1 g sodium citrate, and 100 mL DI water were mixed in a 300-mL round-bottom flask under vigorous stirring. Subsequently, 10 mL (2 M) of NaOH aqueous solution and 10 mL (0.6 M) of ascorbic acid aqueous solution were successively added into the mixed solution slowly. All these procedures were carried out with vigorous magnetic stirring in a water bath at 50 °C. After 3 h of aging for crystals growth, the mixture was centrifuged with water and ethanol to obtain the $Cu_2O$ crystals. In order to control the morphologies of $Cu_2O$ crystals, the amount of PVP in the reaction system was designed to be 0.5 g for C-$Cu_2O$, 3.3 g for C-O-$Cu_2O$ and 8.8 g for O-$Cu_2O$.

### Deposition of Au nanoparticles on the surfaces of $Cu_2O$ crystals

$Cu_2O$ crystals were chosen as the carrier of Au nanoparticles by a simple visible-light irradiation treatment [32]. In brief, 20 mg C-O-$Cu_2O$ crystals were well mixed with 30 mL DI water through ultrasonic treatment, and then, 3 mL (0.5 M) $HAuCl_4$ aqueous solution was added into the above suspension quickly and exposed in visible light for 10 min by using a 300-W xenon lamp assembled with a UV cut-off filter (wave length > 400 nm).

### Synthesis of $Cu_2O$/ZnO p–n heterojunction

$Cu_2O$/ZnO p–n heterojunctions with different $Cu_2O$ crystals (cubic, octahedral and cuboctahedral) and various Zn/Cu molar ratios (1:1, 1:2, 1:3, 1:4 and 1:5 in the precursor solution during preparation process) were synthesized by a simple hydrothermal method. The corresponding $Cu_2O$/ZnO heterojunctions were denoted as C-CZ (cubic $Cu_2O$/ZnO), O-CZ (octahedral $Cu_2O$/ZnO) and C-O-CZ (cuboctahedral $Cu_2O$/ZnO). Taking the Zn/Cu ratio of 1:1 in preparation process as an example, 0.02 g (0.140 mmol) of the above $Cu_2O$ crystals (such as C-O-CZ), 0.5 g of PVP and 24.5 mL of DI water were added into a 50-mL beaker and adequately mixed, and then, 0.5 mL of zinc acetate aqueous solution (0.556 M) was added dropwise under constant stirring, and finally, the suspension was transferred to a 50-mL Teflon-lined stainless steel autoclave and heated at 180 °C for 45 min. The final product was washed with DI water and ethanol by centrifugation and then dried at 70 °C for 3 h. Changing the amount of zinc acetate aqueous solution in the reaction system from 0.5 mL to 0.25, 0.17, 0.125 and 0.1 mL, respectively, the C-O-CZ-x composites with different Zn/Cu molar ratios were finally obtained (x = 1, 2, 3, 4 and 5, respectively).

### Characterization

The morphologies and structures of samples were observed by a scanning electron microscope (SEM, Hitachi S4800) with an EDS (energy-dispersive spectroscopy) detector operated at a voltage of 20 kV and a transmission electron microscope (TEM, Hitachi H-7650) operated at a voltage of 200 kV. The crystalline structure was investigated by an X-ray diffractometer (Bruker AXS D8) using the Cu Kα radiation ($\lambda$ = 0.15418 nm) with the $2\theta$ scan from 10 to 80° at a step of 0.02°. Elemental analysis was performed by X-ray photoelectron spectroscopy (XPS) using a Thermo Fisher Scientific ESCALAB Xi + instrument with an Al Kα radiation source, and the resulting binding energies were calibrated to the C1s (284.6 eV) peak. Inductively coupled plasma optical emission spectroscopy (ICP-OES, Agilent 720ES, America) was used to measure actual content of the

prepared samples. The optical properties of samples were obtained through a Hitachi U-3900 UV–Vis spectrophotometer and a Hitachi F7000 photoluminescence (PL) spectrophotometer at an excitation wavelength of 560 nm.

### Photocatalytic performance measurement

The photocatalytic performance measurement was taken by the photodegradation of MO solution under visible-light irradiation. Concretely, 15 mg catalyst was added into 40 mL (20 mg/L) MO solution in a quartz reactor system. Before irradiation, the suspension was magnetically stirred in dark for 30 min to reach an adsorption–desorption equilibrium. Meanwhile, a blank experiment was also conducted by using this MO solution without adding any catalysts. Subsequently, a 300-W xenon lamp (CEL-HXF300 Beijing Aulight Co., Ltd, China) assembled with a UV cut-off filter (providing visible light > 400 nm) was placed 10 cm away from the suspension as the visible-light source. During irradiation process, the suspension was always under magnetic stirring, and a circulation water-cooling system was used to maintain the temperature of suspension at room temperature. After irradiating every 30 min, 5 mL of the suspension was removed from the photocatalytic system and centrifuged at 3000 rpm for 5 min to remove the catalyst particles from the suspension. The MO concentration in solution was evaluated for the photocatalytic efficiency of the catalyst by measuring the adsorption at 464 nm using a Hitachi U-3900 UV–Vis spectrophotometer at room temperature.

### Active species trapping experiments

Active species trapping experiments were carried out using different scavengers: carbon tetrachloride ($CCl_4$) as $e^-$ scavenger, disodium ethylenediaminetetraacetate (EDTA) as hole scavenger, p-benzoquinone (BQ) as $O_2^-$ scavenger and isopropyl alcohol (IPA) as $OH^-$ scavenger. Typically, 1 mM different scavengers were added into the MO solution, respectively, and the change in MO absorption spectra by the addition of scavenger was used to determine the active species in the photocatalytic reaction.

### Photocurrent measurement

The transient photocurrent measurement was implemented through a CHI660D electrochemical analysis instrument with a standard three-compartment system [4], including a working electrode, a platinum counter electrode and an Ag/AgCl reference electrode. The electrolyte was phosphate buffer saline (PH = 7) aqueous solution, and the irradiation source was a 150-W halogen tungsten lamp with an UV cut-off filter (providing visible light > 400 nm). For the preparation of the working electrode, 20 mg of catalyst, 25 μL of absolute ethanol, 25 μL of DI water and 80 μL of Nafion solution were sonicated to form a viscous slurry. The slurry was then coated on fluorine-doped $SnO_2$ transparent conductive glass (FTO glass) to form a uniform film and heated in vacuum at 80 °C for 4 h.

## Results and discussion

### Morphological and structure of photocatalysts

The morphologies and microstructures of $Cu_2O$ crystals prepared by reducing $Cu^{2+}$ with ascorbic acid in the presence of different amounts of PVP are shown in Fig. 1a–c. It can be seen that the C-$Cu_2O$ crystal has six exposed {100} crystal facets, O-$Cu_2O$ has eight exposed {111} facets and the C-O-$Cu_2O$ has six exposed {100} facets and eight exposed {111} facets. All three types of $Cu_2O$ crystals have relatively regular morphology and dimension uniformity with an average size of about 1 μm. Obviously, with the increase of the amount of PVP in the reaction system, the morphological evolution of $Cu_2O$ crystals is from cube to cuboctahedron and then to octahedron. Due to the difference in electronegativity between Cu and O atoms, the {100} facets of $Cu_2O$ crystals are predominated by only Cu or O atoms, leading to the electrically neutral state of {100} facets. As for the {111} facets, it is composed by both Cu and O atoms, the Cu atoms with dangling bonds on the {111} facets would lead to these facets to be positively charged, so the {111} facets have strong absorption capacity to some negatively charged capping agent, such as PVP [33–36]. As a result, the addition of PVP can inhibit the growth of {111} facets and delay oxidation etching, so that the {111} facets can remain stable after the

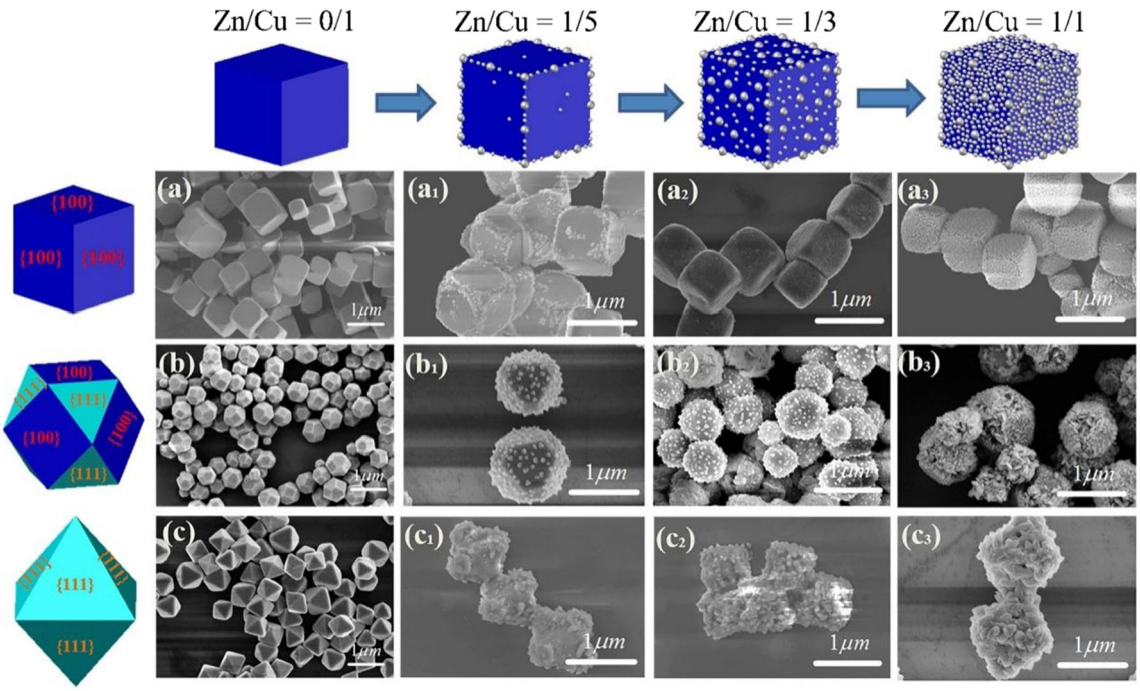


**Figure 1** SEM images of $Cu_2O$ crystals with different morphologies: **a** C-$Cu_2O$, **b** C-O-$Cu_2O$ and **c** O-$Cu_2O$. SEM images of $Cu_2O$/ZnO heterojunctions with different Zn/Cu molar ratios (1:5, 1:3, 1:1) for (a1)–(a3) C-CZ, (b1)–(b3) C-O-CZ and (c1)–(c3) O-CZ heterojunctions, respectively.

synthesis reaction. This feature ensures that we can control the ratio of {100} and {111} facets by controlling the amount of PVP added. In order to verify the above hypothesis, we performed an experiment of visible-light reduction of $[AuCl_4]^-$ ions onto the surfaces of C-O-$Cu_2O$ crystals. The SEM image in Fig. S1 (a) shows that Au nanoparticles preferentially deposit on the {111} facets due to its strong absorption capacity to negatively charged $[AuCl_4]^-$ ions. The XRD patterns in Fig. S1 (b) show the characteristic diffraction peaks of Au with {111} and {311} planes located at 38.2°and 77.5°, respectively, which indicates that the photogenerated electrons of $Cu_2O$ are selectively concentrated on the {111} high-energy facets, and holes tend to shift to the low-energy {100} facets. The accumulated electrons on {111} facets favor the nucleation and growth of Au nanoparticles, indicating that the coexists of {100} and {111} facets are beneficial for the efficient separation of electron–hole pairs [30]. Therefore, we may get the conclusion that the catalytic activity of the $Cu_2O$ crystals follows the order as C-O-$Cu_2O$ > O-$Cu_2O$ > C-$Cu_2O$.

When zinc acetate aqueous solution was added into the hydrothermal reaction, $Cu_2O$/ZnO p–n heterojunctions with different Zn/Cu molar ratios were obtained. As shown in Fig. 1($a_1$) to Fig. 1($c_3$), with the increase of the $Zn^{2+}$ precursor, the ZnO nanoparticles distributed on the surface of the $Cu_2O$ crystal gradually increase and basically cover the surface of the $Cu_2O$ crystal. For C-CZ crystals, the edges and corners are low-energy crystal facets of {100}, which do not produce preferential deposition effects. For C-O-CZ and O-CZ heterojunctions, since their exposed {111} facets are relatively high-energy crystal facets, ZnO nanoparticles are preferentially deposited on the high-energy edges and corners of the $Cu_2O$ crystals [37]. This further confirms the hypothesis that the {111} facets have higher catalytic activity.

Figure 2 shows the TEM and high-resolution TEM (HR-TEM) images of C-CZ heterojunction with Zn/Cu molar ratio of 1:3 (C-CZ-3 heterojunction). The average sizes of $Cu_2O$ crystals and ZnO nanoparticles are 1 μm and 4 nm, respectively (Fig. 2a). The HR-TEM image of Fig. 2b shows that the lattice fringe spacing of 0.247 nm corresponds to the {111} plane of $Cu_2O$, and the lattice fringe spacing of 0.191 nm in semiconductor domain is consistent with the (102) facet of hexagonal wurtzite ZnO. The results demonstrate that the close contact between the two

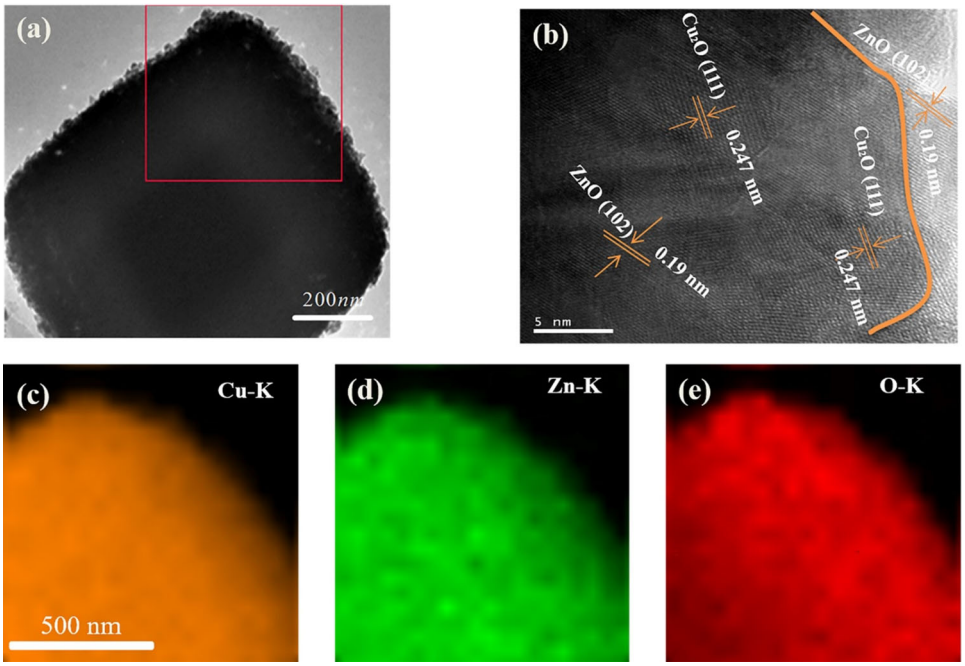


**Figure 2** **a** TEM and **b** HR-TEM images of C-CZ-3 heterojunction. The corresponding EDS mapping images of **c** Cu, **d** Zn and **e** O elements.

components at the heterojunction interface is formed, which may facilitate the transfer of photogenerated electron at the interfaces. In addition, the EDS mapping of p–n heterojunctions is also studied, indicating the existence of Cu, Zn and O elements and their uniform distribution (Fig. 2c-e).

Figure 3 shows the XRD patterns of pure $Cu_2O$ crystals and O-CZ heterojunctions. The diffraction peaks of $Cu_2O$ crystals with different morphologies are similar (Fig. 3a), and all characteristic diffraction peaks belong to face-centered cubic $Cu_2O$ single crystal (JCPDS card NO. 05–0667), and no characteristic peaks related to CuO or Cu crystals are found [38]. The peak intensity of {111} crystal planes at $2\theta = 36.4°$ increases sequentially when the morphologies of $Cu_2O$ crystals change from cube to cuboctahedron and finally to octahedron. We also investigated the XRD patterns of O-CZ heterojunctions with different Zn/Cu molar ratios. As shown in Fig. 3b, with the increasing molar ratio of Zn/Cu from 1:1 to 1:5, the XRD patterns from O-CZ-1 to O-CZ-5 are complete with no change, indicating that the structure of O-$Cu_2O$ crystals is well preserved when the heterojunction is formed. We can also find the characteristic diffraction peaks of hexagonal wurtzite ZnO (JCPDS card No. 36–1451) [39] from O-CZ heterojunctions at 31.8, 34.2, 47.5, 56.5 and 66.4°, and these diffraction peak intensities gradually decrease when the Zn/Cu molar ratio decreases from 1:1 to 1:5, which indicates the easy control of ZnO nanoparticles well decorated on the surface of $Cu_2O$ crystals.

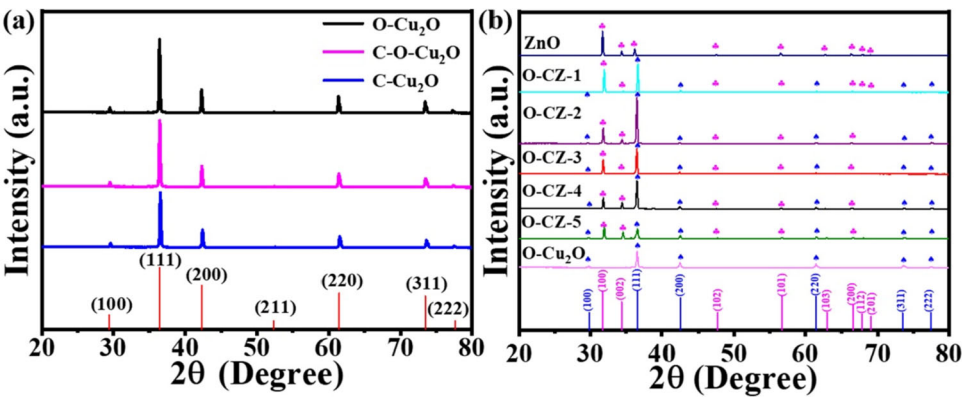


**Figure 3** XRD patterns of **a** pure $Cu_2O$ crystals with different morphologies and **b** ZnO and O-CZ heterojunctions with different Zn/Cu molar ratios.

The XPS spectra of O-CZ-3 heterojunctions were further measured, and the high-resolution XPS spectra show that the binding energies of Cu $2p_{3/2}$ and Zn $2p_{3/2}$ are about 932.6 and 1021.8 eV, respectively (Fig. 4). The EDS image of O-CZ-3 heterojunction is shown in Fig. S2, giving a proportional relationship of Zn/Cu about 1:3.17. This results are similar to the elemental contents of $Cu_2O$/ZnO heterojunction samples via the ICP-OES measurement (Table S1) in Supporting Information. The experimental results indicate that molar ratios of Zn/Cu in the $Cu_2O$/ZnO p–n heterojunctions slightly lower than those in precursors due to possible loss of source material in the reaction process.

## Photoluminescence and photocurrent properties of photocatalysts

Figure 5a displays the PL spectra of O-CZ with different Zn/Cu molar ratios. The intensity of PL peaks at ~ 605 nm presents a tendency to increase and then decrease with the maximum obtained from O-CZ-3. This can be attributed to the suppressed recombination of photogenerated electron–hole pairs after ZnO loading on the surface of $Cu_2O$. However, when loading amount of ZnO is too much, the accumulated ZnO affects the transmission path of photogenerated electron–hole pairs, causing the increase in recombination rate and the decrease in PL peak intensity. Therefore, the preferred Zn/Cu molar ratio is 1:3. The transient photocurrent characterization also confirms this view. As shown in Fig. 5b, the highest photocurrent response is obtained for the O-CZ-3 heterojunction with the Zn/Cu molar ratio of 1:3, hinting its lowest electron–hole pair recombination rate and optimal catalytic activity.

## Photocatalytic degradation of methyl orange

The catalytic performance of pure $Cu_2O$ crystals and $Cu_2O$/ZnO p–n heterojunctions was investigated by degradation experiments of MO under visible-light illumination, and the adsorption peaks of MO at 464 nm in the presence of different photocatalysts under visible-light irradiation are shown in Fig. S3. The curves of the MO degradation percent as a function of time are shown in Fig. 6. Before visible-light irradiation, the suspension containing MO and catalysts is magnetically stirred in darkness for 30 min to achieve an adsorption–desorption equilibrium (Fig. 6a). In the case of the absence of catalyst, the concentration of MO solution is almost unchanged after a period of 150-min visible-light irradiation, indicating the self-degradation of MO solution can be ignored. The difference in the catalytic performances of $Cu_2O$ crystals with different morphologies follows the order of C-O-$Cu_2O$ > O-$Cu_2O$ > C-$Cu_2O$. These experiment results are consistent with our previous hypothesis, that is, the catalytic performance of $Cu_2O$ crystals is facet dependent, and C-O-$Cu_2O$ composed of {111} and {100} facets exhibits better catalytic activity than the other two kinds of $Cu_2O$ crystals. The different catalytic performance originates form the number of terminal copper atoms per unit surface of different facets [29, 40], so theoretically the $Cu_2O$ crystals with {111} facets exposed would possess a better catalytic activity than the $Cu_2O$ crystals with {100} facets exposed due to the more aggregation of terminal copper atoms on the {100} facets. More importantly, the coexistence of {111} and {100} planes of C-O-$Cu_2O$ crystals can induce better separation of electron–hole pairs due to the slight difference in energy levels between the two planes; thus, the photogenerated electrons selectively aggregate on the

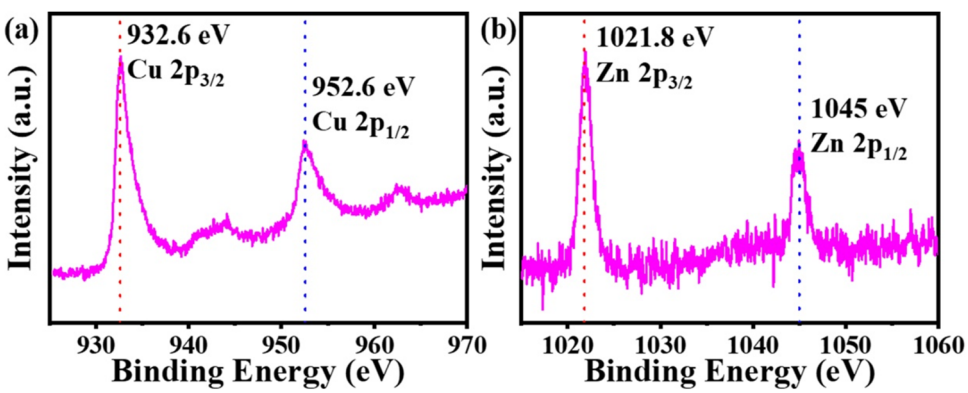


**Figure 4** XPS spectra of **a** Cu 2p core level and **b** Zn 2p core level for O-CZ-3 heterojunctions.

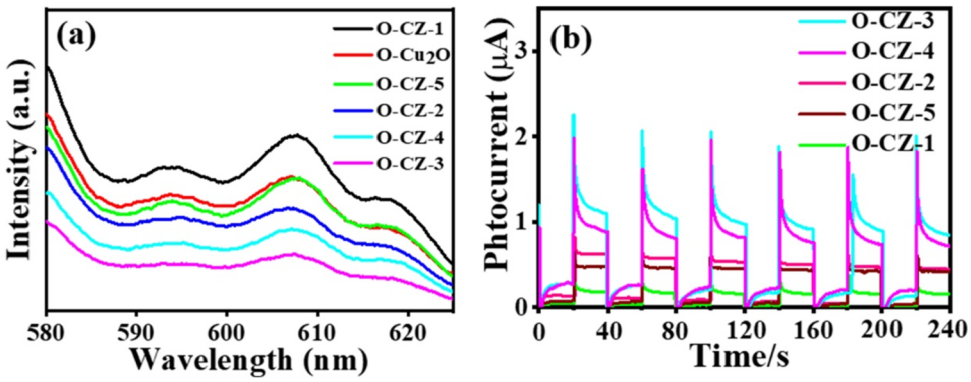


**Figure 5** **a** PL spectra of O-$Cu_2O$ and O-CZ heterojunctions with different Zn/Cu molar ratios from 1:1 to 1:5; **b** photocurrent responses of O-CZ heterojunctions with different Zn/Cu molar ratios in the visible-light on–off process at a potential of 0 V vs saturated Ag/AgCl electrode..

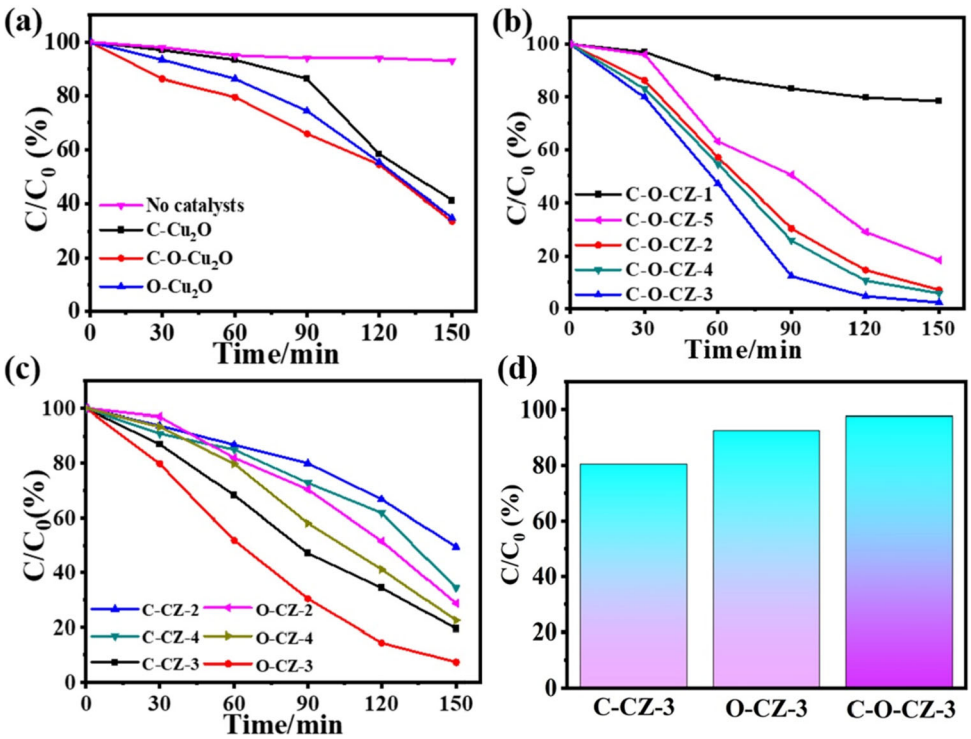


**Figure 6** Residual MO percentage versus visible-light irradiation treatment time for **a** $Cu_2O$ crystals with three morphologies, **b** C-O-CZ heterojunctions with different Zn/Cu molar ratios from 1:1 to 1:5, C-CZ and **c** O-CZ heterojunctions with Zn/Cu molar ratios from 1:2 to 1:4, **d** degradation rate of MO C-CZ-3, O-CZ-3 and C-O-CZ-3 heterojunctions after 150-min visible-light irradiation.

{111} facets, and holes tend to shift to the {100} facets [30], resulting in the better catalytic activity of C-O-$Cu_2O$ crystals than the O-$Cu_2O$ and C-$Cu_2O$ crystals (Fig. 6a).

Considering that MO is an anionic dye, thus the surface charge of the photocatalyst is an important influencing factor for the adsorption and photocatalytic degradation of MO. The adsorption experiments before adsorption–desorption equilibrium without light irradiation are shown in Table S2 in Supporting Information, which shows that with the deposition of appropriate amount of ZnO in the C-O-CZ heterojunction, it is helpful to adsorb anionic MO, while excessive ZnO is not conducive to the adsorption of MO because of electronic repulsion [41, 42]. Obviously, the dye concentration adsorbed without light irradiation depends on the Zn/Cu molar ratio of $Cu_2O$/ZnO p–n heterojunctions. Therefore, we set the concentration of MO at adsorption–desorption equilibrium point as the normalized initial concentration $C_0$. From the catalytic performance curves of the C-O-CZ heterojunctions with various Zn/Cu molar ratios in Fig. 6b, it can be seen that after 150 min of visible-light irradiation, the degradation effect of the C-O-CZ heterojunction has a significantly improvement than pure $Cu_2O$ crystal, especially the C-O-CZ-3 heterojunction, the degradation rate reaches ~ 98%. This indicates that the formation of $Cu_2O$/ZnO p–n heterojunctions accelerates the transfer of photoinduced electrons from $Cu_2O$ to

ZnO, which increases the lifetime of the carriers and thus improves the catalytic efficiency. However, superfluous deposition of ZnO nanoparticles onto $Cu_2O$ surface decreases the contact area between $Cu_2O$ and the MO solution to some extent, and not enough photoinduced carriers can be formed at the limited active sites, hindering the catalytic degradation of MO. The effect of $Cu_2O$ morphology and Zn/Cu molar ratios on catalytic performances of C-CZ and O-CZ heterojunctions is also explored into and compared with the results of C-O-CZ heterojunctions (Figs. 6c and 6d), verifying the controllability of photocatalytic performances by designing the crystal structure and content of catalysts. Our results indicate that the order of catalytic efficiency follows C-O-CZ > O-CZ > C-CZ.

## Reusability of photocatalytic

In addition to photocatalytic activity, the sustainability and stability of $Cu_2O$/ZnO p–n heterojunctions are very important for their practical applications. As shown in Fig. 7a, the data curves of the MO degradation percent after five cycles of catalytic experiments under the identical circumstances have been obtained for the O-CZ-3 heterojunction as a reference. After five-cycle experiments, the catalytic effect of O-CZ-3 heterojunctions almost remains unchanged. The SEM images show that the ZnO nanoparticles are firmly anchored on the surface of $Cu_2O$, and the O-CZ-3 heterojunctions still maintain good morphology and stability after five cycles. Weak characteristic peaks related to CuO appear in the XRD pattern due to the slight oxidation of $Cu_2O$ to form CuO on the surface of $Cu_2O$. The generation of the thin CuO layer can prevent the further oxidation of $Cu_2O$, thus ensuring the stability of the $Cu_2O$/ZnO heterojunction. On the other hand, the presence of ZnO promotes the rapid transfer of photoelectrons and holes, which can also delay the occurrence of photocorrosion [43].

## Photocatalytic degradation mechanism of MO on $Cu_2O$/ZnO heterojunction

The photocatalytic degradation mechanism of $Cu_2O$/ZnO for the target pollutants is shown in Fig. 8a. ZnO is a typical n-type semiconductor with a band gap of about 3.3 eV, whereas $Cu_2O$ is a typical p-type semiconductor with a band gap of about 2.2 eV [43, 44]. When these two materials are combined together to form a p–n heterojunction catalyst, there is a significant band energy shift between the two materials, with electrons diffusing from the Fermi level of ZnO to $Cu_2O$, leading to the accumulation of negative charges in the $Cu_2O$ junction region and the formation of positive charges over ZnO until their Fermi levels reach equilibrium [45, 46]. Due to the presence of n-type ZnO with a positive charge and p-type $Cu_2O$ with a negative charge, an internal electric field can be formed in the depletion layer, which can provide an internal driving force that drives the transfer of photogenerated electrons from the narrow bandgap semiconductor $Cu_2O$ to ZnO, while the photogenerated holes remain on the VB of $Cu_2O$ [12, 47, 48]. As a result, the photoinduced electrons and holes are efficiently separated from each other and their recombination is prolonged.

Moreover, in order to investigate the role of active species during the photocatalytic degradation of MO, the active species trapping tests were performed using four different scavengers to identify the main active species involved in the photocatalytic degradation experiments. $CCl_4$, EDTA, BQ and IPA were

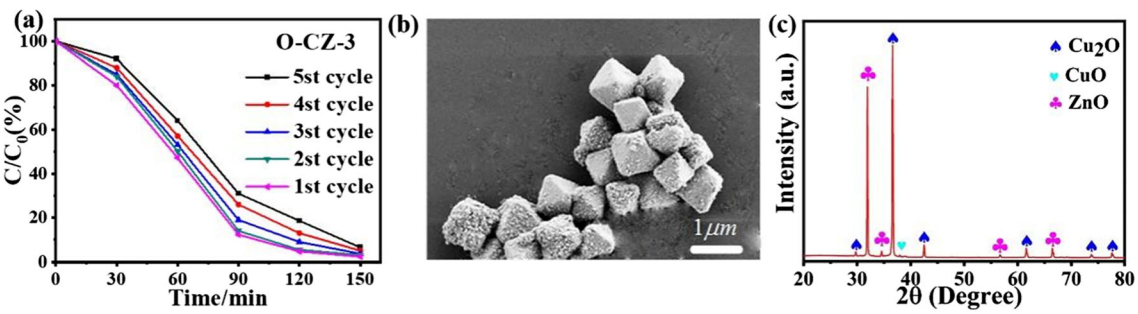


**Figure 7** **a** Photodegradation test of MO by using O-CZ-3 heterojunction for five cycles, **b** corresponding SEM image and **c** XRD spectrum of O-CZ-3 heterojunction after five-cycle measurements.

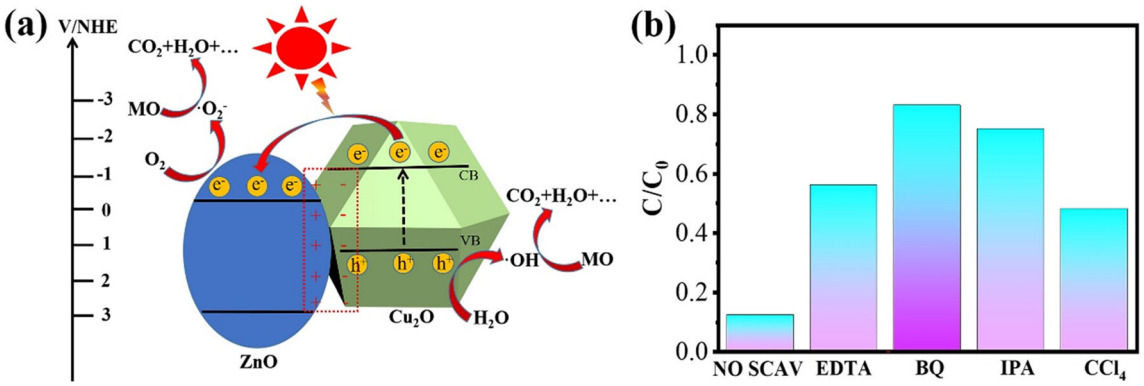


**Figure 8** **a** Photocatalytic degradation mechanism of MO by using $Cu_2O$/ZnO p–n heterojunctions under visible-light irradiation. **b** The active species trapping experiments for photocatalytic degradation of MO over O-CZ-3 heterojunction.

added into the suspension of MO as scavengers for $e^-$, $h^+$, $\cdot O_2^-$ and ·OH, respectively. Take O-CZ-3 heterojunction as an example, the effect of scavengers on the reactive species in the process of catalytic reaction is displayed in Fig. 8b. After the solution with O-CZ-3 heterojunction is visible-light irradiated for 90 min, BQ and IPA are introduced, and the photocatalytic degradation of MO is remarkably suppressed, indicating that the $\cdot O_2^-$ and ·OH are the main reactive species for degradation. In addition, the presence of $CCl_4$ and EDTA has slight inhibitory effect, which implies that $e^-$ and hole are also responsible for the degradation of MO. The photodegradation of MO using $Cu_2O$/ZnO p–n heterojunctions can be described as

$$Cu_2O + h\upsilon \rightarrow Cu_2O\left(h^+ + e^-\right) \quad (1)$$

$$Cu_2O\ (e^-) \xrightarrow{\text{transfer}} ZnO\ (e^-) \quad (2)$$

$$ZnO\ (e^-) + O_2 \rightarrow ZnO + \cdot O_2^- \quad (3)$$

$$H_2O + Cu_2O\left(h^+\right) \rightarrow \cdot OH + H^+ \quad (4)$$

$$O_2^- + MO \rightarrow CO_2 + H_2O + \ldots \quad (5)$$

$$\cdot OH^- + MO \rightarrow CO_2 + H_2O + \ldots \quad (6)$$

Through the above characterization and experimental results, it can be concluded that decorating a certain proportion of ZnO nanoparticles on the surface of $Cu_2O$ to form a p–n heterojunction can effectively improve the catalytic activity and stability. Among the three crystal face-dependent $Cu_2O$ with different morphologies, the C-O-$Cu_2O$ with {111} and {100} planes exhibits more outstanding catalytic performance because the energy-level difference between {111} and {100} planes of C-O-$Cu_2O$ leads to electron–hole pair separation faster than C-$Cu_2O$ composed of {100} planes and O-$Cu_2O$ composed of {111} planes.

## Conclusion

In summary, a simple preparation strategy for $Cu_2O$/ZnO heterojunctions with cube, cuboctahedron and octahedron morphologies is designed and realized by a rapid hydrothermal method. The decoration density of ZnO nanoparticles can be adjusted by changing the adding amount of $Zn^{2+}$ precursors. It is shown that the photocatalytic efficiency of the prepared $Cu_2O$/ZnO heterojunctions relies not only on the construction of p–n junctions but also on the morphologies of $Cu_2O$ crystals and the coverage density of ZnO nanoparticles. Through the experimental analysis, we can find that photocatalytic efficiency of the p–n junction increases with increasing the coverage density of ZnO nanoparticles; however, when the loading capacity of ZnO nanoparticles reaches a certain degree, the agglomerated ZnO nanoparticles cover the active sites of $Cu_2O$ crystals and, meanwhile, act as recombination sites for photogenerated electron–hole pairs, reducing the catalytic capacity of $Cu_2O$/ZnO heterojunctions. Therefore, reasonable controlling for the morphology of $Cu_2O$ crystal, the loading capacity of ZnO nanoparticles and p–n junctions structure is vital for the improvement in catalytic efficiency of $Cu_2O$/ZnO heterojunction catalysts.

## Acknowledgements

This work was supported by the National Natural Science Foundation of China (Nos. 12272351, 11672269 and 11972323), the Zhejiang Outstanding Youth Fund of China (No. LR19E020004), the Youth Top-notch Talent Project of Zhejiang Ten Thousand Plan of China (No. ZJWR0308010), the Zhejiang Provincial Natural Science Foundation of China (Nos. LR20A020002 and LQ20E010009) and the Fundamental Research Funds of Zhejiang Sci-Tech University (2021Q050).

## Declarations

**Conflict of interest** The authors declare that they have no conflict of interest.

**Supplementary Information:** The online version contains supplementary material available at https://doi.org/10.1007/s10853-022-08059-x.

## References

[1] Zhang Y, Liu MM, Chen J, Fang S, Zhou P (2021) Recent advances in $Cu_2O$-based composites for photocatalysis: a review. Dalton Trans 50:4091–4111

[2] Dong S, Wang Y, Liu Z, Zhang W, Yi K, Zhang X, Zhang X, Jiang C, Yang S, Wang F, Xiao X (2020) Beehive-inspired macroporous SERS probe for cancer detection through capturing and analyzing exosomes in plasma. ACS Appl Mater Interfaces 12:5136–5146

[3] Bai W, Wu M, Du X, Gong W, Ding Y, Song C, Liu L (2021) Synergistic effect of multiple-phase rGO/CuO/$Cu_2O$ heterostructures for boosting photocatalytic activity and durability. Appl Surf Sci 544:148607

[4] Jing L, Li H, Yan X, Fang H, Wei W (2014) Facile electrodeposition of environment-friendly $Cu_2O$/ZnO heterojunction for robust photoelectrochemical biosensing. Sens Actuators B Chem 191:619–624

[5] Wang Y, Gao T, Wang K, Wu X, Shi X, Liu Y, Lou S, Zhou S (2012) Template-assisted synthesis of uniform nanosheet-assembled silver hollow microcubes. Nanoscale 4:7121–7126

[6] Sun S, Zhang X, Yang Q, Liang S, Zhang X, Yang Z (2018) Cuprous oxide ($Cu_2O$) crystals with tailored architectures: a comprehensive review on synthesis, fundamental properties, functional modifications and applications. Prog Mater Sci 96:111–173

[7] Ren S, Wang B, Hui Z, Peng D, Qiang W (2015) Sandwiched ZnO@ Au@ $Cu_2O$ nanorod films as efficient visible-light-driven plasmonic photocatalysts. ACS Appl Mater Interfaces 7:4066–4074

[8] Ren ST, Fan GH, Liang ML, Wang Q, Zhao GL (2014) Electrodeposition of hierarchical ZnO/$Cu_2O$ nanorod films for highly efficient visible-light-driven photocatalytic applications. J Appl Phys 115:064301

[9] Yu X, Chen H, Ji Q, Chen Y, Yao B (2021) p-$Cu_2O$/n-ZnO heterojunction thin films with enhanced photoelectrochemical properties and photocatalytic activities for norfloxacin. Chemosphere 267:129285

[10] Rajendran R, Vignesh S, Sasireka A, Priya P, Suganthi S, Raj V, Sundar JK, Srinivasan M, Shkir M, AlFaify S (2021) Investigation on novel $Cu_2O$ modified g-$C_3N_4$/ZnO heterostructures for efficient photocatalytic dye degradation performance under visible-light exposure. Colloids Interface Sci Commun 44:100480

[11] Wang Y, Kai GKC, Xiao D, Zhu J, Shu X, Ping LC, Man YK (2022) Improving the p-type conductivity of $Cu_2O$ thin films by Ni doping and their heterojunction with n-ZnO. Appl Surf Sci 590:153047

[12] Pirhashemi M, Habibi-Yangjeh A (2016) Photosensitization of ZnO by AgBr and $Ag_2CO_3$: nanocomposites with tandem n-n heterojunctions and highly enhanced visible-light photocatalytic activity. J Colloid Interface Sci 474:103–113

[13] Chen J, Zhang X, Shi X, Bi F, Yang Y, Wang Y (2020) Synergistic effects of octahedral $TiO_2$-MIL-101 (Cr) with two heterojunctions for enhancing visible-light photocatalytic degradation of liquid tetracycline and gaseous toluene. J Colloid Interface Sci 579:37–49

[14] Das D, Makal P (2020) Narrow band gap reduced $TiO_2$-B: Cu nanowire heterostructures for efficient visible light absorption, charge separation and photocatalytic degradation. Appl Surf Sci 506:144880

[15] Wannapop S, Somdee A (2022) Highly orientated one-dimensional $Cu_2O/TiO_2$ heterostructure thin film for photoelectrochemical photoanode and photocatalytic degradation applications. Thin Solid Films 747:139144

[16] Pan J, Li S, Liu Y, Ou W, Li C (2020) The flexible-transparent p n junction film device of N-doped $Cu_2O/SnO_2$ orderly nanowire arrays towards highly photovoltaic conversion and stability. Chem Eng J 382:122813

[17] Zhao Y, Yin H, Fu Y, Wang X, Wu W (2019) Energy band alignment at $Cu_2O$/ZnO heterojunctions characterized by in situ x-ray photoelectron spectroscopy. Chin Phys B 28:087301

[18] Zhang G, Zhao J, Yang T, Zhang Q, Zhang L (2021) In-situ self-assembled $Cu_2O$/ZnO core-shell catalysts synergistically

enhance the durability of methanol steam reforming. Appl Catal A Gen 616:118072

[19] Abdolhoseinzadeh A, Sheibani S (2020) Enhanced photocatalytic performance of $Cu_2O$ nano-photocatalyst powder modified by ball milling and ZnO. Adv Powder Technol 31:40–50

[20] Ibrahim MM, Mezni A, El-Sheshtawy HS, Abu Zaid AA, Alsawat M, El-Shafi N, Ahmed SI, Shaltout AA, Amin MA, Kumeria T (2019) Direct Z-scheme of $Cu_2O/TiO_2$ enhanced self-cleaning, antibacterial activity, and UV protection of cotton fiber under sunlight. Appl Surf Sci 479:953–962

[21] Sajan CP, Wageh S, Al-Ghamdi AA, Yu JG, Cao SW (2016) $TiO_2$ nanosheets with exposed 001 facets for photocatalytic applications. Nano Res 9:3–27

[22] Li J, Ni Z, Ji Y, Zhu Y, Su F (2019) ZnO supported on $Cu_2O$ 1 0 0 enhances charge transfer in dimethyldichlorosilane synthesis. J Catal 374:284–296

[23] Mohammed AM, Mohtar SS, Aziz F, Aziz M, Ul-Hamid A (2021) $Cu_2O$/ZnO-PANI ternary nanocomposite as an efficient photocatalyst for the photodegradation of Congo Red dye. J Environ Chem Eng 9:105065

[24] Zemzemi M, Alaya S (2013) Band offset of the ZnO/$Cu_2O$ heterojunction from ab initio calculations. Superlattices Microstruct 64:311–318

[25] Kaur R, Suresh M, Vidrier JL, Gutsch S, Weiss C, Prescher M, Kirste L, Singh R, Pal B, Zacharias M (2020) In situ approach to fabricate heterojunction p-n CuO-ZnO nanostructures for efficient photocatalytic reactions. New J Chem 44:19742–19752

[26] Basu M, Garg N, Ganguli AK (2014) A type-II semiconductor (ZnO/CuS heterostructure) for visible light photocatalysis. J Mater Chem A 2:7517–7525

[27] Yu X, Ji Q, Wei Y, Liu Z, Zhao N, Yang M, Yang Q (2021) Preparation of Novel ZnO/$Cu_2O$ heterojunctions composite film by codeposition method and their enhanced photocatalytic performance analysis. J Electrochem Soc 168:126513

[28] Mohammed AM, Mohtar SS, Aziz F, Aziz M, Ul-Hamid A, Salleh WNW, Yusof N, Jaafar J, Ismail AF (2021) Ultrafast degradation of Congo Red dye using a facile one-pot solvothermal synthesis of cuprous oxide/titanium dioxide and cuprous oxide/zinc oxide pn heterojunction photocatalyst. Mater Sci Semicond Process 122:105481

[29] Huang WC, Lyu LM, Yang YC, Huang MH (2012) Synthesis of $Cu_2O$ nanocrystals from cubic to rhombic dodecahedral structures and their comparative photocatalytic activity. J Am Chem Soc 134:1261–1267

[30] Zhang L, Shi J, Liu M, Jing D, Guo L (2014) Photocatalytic reforming of glucose under visible light over morphology controlled $Cu_2O$: efficient charge separation by crystal facet engineering. ChemComm 50:192–194

[31] Zhang DF, Hua Z, Lin G, Zheng K, Zhang Z (2009) Delicate control of crystallographic facet-oriented $Cu_2O$ nanocrystals and the correlated adsorption ability. J Mater Chem 19:5220–5225

[32] Cui C, Wang Y, Liang D, Cui W, Hu H, Lu B, Xu S, Li X, Wang C, Yang Y (2014) Photo-assisted synthesis of $Ag_3PO_4$/reduced graphene oxide/Ag heterostructure photocatalyst with enhanced photocatalytic activity and stability under visible light. Appl Catal B 158:150–160

[33] Xydou A, Parviainen S, Djurabekova F (2020) Diffusion bonding of Cu atoms with molecular dynamics simulations. Results Phys 16:102890

[34] Lou Y, Zhang Y, Cheng L, Chen J, Zhao Y (2018) A stable plasmonic Cu@$Cu_2O$/ZnO heterojunction for enhanced photocatalytic hydrogen generation. Chemsuschem 11:1505–1511

[35] Jain S, Mishra S, Sarma TK (2018) Zn2+ induced self-assembled growth of Octapodal $Cu_xO$-ZnO microcrystals: multifunctional applications in reductive degradation of organic pollutants and nonenzymatic electrochemical sensing of glucose. ACS Sustain Chem Eng 6:9771–9783

[36] Gao Y, Wu Q, Liang X, Wang Z, Zheng Z, Wang P, Liu Y, Dai Y, Whangbo M, Huang B (2020) Cu2O nanoparticles with both 100 and 111 facets for enhancing the selectivity and activity of $CO_2$ electroreduction to Ethylene. Adv Sci 7:1902820

[37] Saeid MP, Kong EYJ, Dasineh KN, Reza K, Xiao G (2018) Aluminum-incorporated p-CuO/n-ZnO photocathode coated with nanocrystal-engineered $TiO_2$ protective layer for photoelectrochemical water splitting and hydrogen generation. J Mater Chem A 6:11951–11965

[38] Pawar SM, Kim J, Inamdar AI, Woo H, Im H (2016) Multifunctional reactively-sputtered copper oxide electrodes for supercapacitor and electro-catalyst in direct methanol fuel cell applications. Sci Rep 6:1–9

[39] Al Abdullah K, Awad S, Zaraket J, Salame C (2017) Synthesis of ZnO nanopowders by using sol-gel and studying their structural and electrical properties at different temperature. Energy Procedia 119:565–570

[40] Wu SC, Tan CS, Huang MH (2017) Strong facet effects on interfacial charge transfer revealed through the examination of photocatalytic activities of various $Cu_2O$-ZnO heterostructures. Adv Funct Mater 27:1604635

[41] Chen J, Xiong Y, Duan M, Li X, Li J, Fang SW, Qin S, Zhang R (2020) Insight into the synergistic effect of adsorption-photocatalysis for the removal of organic dye pollutants by Cr-doped ZnO. Langmuir 36:520–533

[42] Yu WB, Liu J, Yi M, Yang JX, Dong WD, Zhao H, Mohamed H, Wang Z, Chen LH, Li Y, Su BL (2020) Active faceted $Cu_2O$ hollow nanospheres for unprecedented

adsorption and visible-light degradation of pollutants. J Colloid Interface Sci 565:207–217

[43] Kandjani AE, Sabri YM, Periasamy SR, Zohora N, Amin MH, Nafady A, Bhargava SK (2015) Controlling core/shell formation of nanocubic p-$Cu_2O$/n-ZnO toward enhanced photocatalytic performance. Langmuir 31(39):10922–10930

[44] Taddesse AM, Alemu M (2020) Enhanced photocatalytic activity of p-n-n heterojunctions ternary composite $Cu_2O$/ZnO/$Ag_3PO_4$ under visible light irradiation. J Environ Chem Eng 8:104356

[45] Yassin JM, Taddesse AM, Sánchez-Sánchez M (2022) Sustainable synthesis of a new semiamorphous Ti-BDC MOF material and the photocatalytic performance of its ternary composites with $Ag_3PO_4$ and g-$C_3N_4$. Appl Surf Sci 578:151996

[46] Yassin JM, Taddesse AM, Sánchez-Sánchez M (2022) Sustainable synthesis of semicrystalline Zr-BDC MOF and heterostructural $Ag_3PO_4$/Zr-BDC/g-$C_3N_4$ composite for photocatalytic dye degradation. Catal Today 390:162–175

[47] Pirhashemi M, Habibi-Yangjeh A (2018) ZnO/$NiWO_4$/$Ag_2CrO_4$ nanocomposites with p-n-n heterojunctions: highly improved activity for degradations of water contaminants under visible light. Sep Purif Technol 193:69–80

[48] Taddesse AM, Bekele T, Diaz I, Adgo A (2021) Polyaniline supported CdS/$CeO_2$/$Ag_3PO_4$ nanocomposite: an "AB" type tandem n-n heterojunctions with enhanced photocatalytic activity. J Photoch Photobio A 406:113005